



# Selective Stereochemical Catalysis Controlled by Specific Atomic Arrangement of Ordered Alloys

Shinya Furukawa,\* Kazuyoshi Ochi, Hui Luo, Masayoshi Miyazaki, and Takayuki Komatsu\*<sup>[a]</sup>

Unprecedented surface stereochemistry governed by specific atomic arrangement of intermetallic compounds (ordered alloys) is shown. Hydrogen-mediated *cis*–*trans* alkene isomerization is selectively catalyzed without overhydrogenation to alkanes by Rh-based intermetallic compounds displaying an orthorhombic *Pnma* structure such as RhSb. Multiple characterization techniques combined with DFT calculations revealed that (211), (020), and (013) planes comprising one-dimension-

ally aligned Rh rows separated by Sb atoms (1D-planes) dominated RhSb surfaces. Systematic DFT calculations indicated that geometric constraints of these 1D-planes and steric hindrance from one alkyl group of *cis*-alkene limited hydrogen access to the alkenyl carbon to one direction, enabling one-atom hydrogenation for isomerization, but inhibiting two-atom hydrogenation for overhydrogenation.

## Introduction

Stereochemical transformations such as enantio, diastereo, and regioselective conversions play key roles in numerous fields including organic chemistry, pharmacology, enzymology, and industrial chemistry. Achieving these sophisticated transformations by simple and catalytic artificial methods continues to be an intriguing area of research.<sup>[1]</sup>

The development of an efficient catalyst for stereoselective conversions generally requires a well-designed reaction environment such as metal complexes bearing tailor-made organic ligands.<sup>[2]</sup> In contrast, inorganic heterogeneous catalysts typically do not provide well-structured reaction sites because of their heterogeneity, but offer potential advantages for practical use such as durability, separability, and reusability. To introduce such a well-structured reaction site to heterogeneous catalysts, appropriate functionalizing organic molecules or metal complexes are immobilized<sup>[3]</sup> or co-adsorbed<sup>[4]</sup> on the catalyst surface. In this context, it is highly challenging to design effective inorganic materials catalyzing stereochemical transformations without the aid of organic components. Although micro or mesoporous inorganic materials such as zeolites have been utilized for stereo<sup>[5]</sup> and regioselective reactions,<sup>[6]</sup> their properties relies on physical restriction by the pore wall typically in nano- or mesoscale. Ideally, a reaction site displaying regularity at the Angstrom-scale and achieving accurate molecular recognition through chemical interactions is more appealing than these materials.

Intermetallic compounds (ordered alloys) present specific crystal structures and, thus, well-defined atomic arrangements of their metal components<sup>[7]</sup> making them attractive candidates for simple and ordered inorganic materials. Their highly ordered bimetallic surface may provide an appropriate reaction environment for controlling stereochemical transformations. A simple geometric effect, dilution or isolation of active metals by their inert metal counterpart (so-called ensemble effect), has been known to inhibit undesired side reactions; for example, Pt–Sn for alkane dehydrogenation<sup>[8]</sup> and Pd–Ga for alkyne semihydrogenation.<sup>[9]</sup> This effect, however, does not contribute to surface stereochemistry. To this day, no one has reported stereochemical conversion governed by surface order. Therefore, developing and understanding such a catalytic system is highly innovative and will open new horizons for stereochemical catalysis, surface science, and materials science.

We recently showed that SiO<sub>2</sub>-supported intermetallic RhSb exhibited the highest selectivity in the hydrogen-mediated catalytic *cis*–*trans* isomerization of stilbene (ST) compared to various Rh-based intermetallic compounds and monometallic Rh.<sup>[10]</sup> Hydrogen-mediated alkene isomerization generally requires a reversible one-atom hydrogenation enabling C–C rotation, but must avoid the irreversible two-atom hydrogenation producing alkane. Therefore, the ordered atomic arrangement of the intermetallic compound likely exerts a specific stereochemical effect on the hydrogenation. However, the nature of the catalysis remains entirely unknown.

In this study, the origin of the specific catalytic properties of RhSb and other intermetallic compounds was investigated in detail in terms of space group and surface atomic arrangement using multiple characterization techniques and density functional theory (DFT) calculations. Herein, we introduce an innovative concept in stereochemical conversion, in which specific atomic arrangement of an ordered alloy governs surface stereochemistry and selective catalysis.

[a] Dr. S. Furukawa, K. Ochi, H. Luo, M. Miyazaki, Prof. T. Komatsu  
Department of Chemistry  
Graduate School of Science and Engineering  
Tokyo Institute of Technology  
2-12-1-E1-10, Ookayama, Meguro-ku, Tokyo, 152-8550 (Japan)  
Fax: (+81)3-3753-2602  
E-mail: komatsu.t.ad@m.titech.ac.jp

Supporting information for this article is available on the WWW under <http://dx.doi.org/10.1002/cctc.201500808>.

## Results and discussion

Monometallic and intermetallic Rh-based catalysts displaying different space groups ( $Fm\bar{3}m$  (Rh),  $Pm\bar{3}m$  (RhGa, RhIn, RhZn),  $Pnma$  (RhGe, RhSb),  $P6/mmm$  (RhPb)) were synthesized by successive impregnation using  $\text{SiO}_2$  as a support. Intermetallic compound RuSb presenting the same crystal structure as RhSb was also prepared. X-ray diffraction (XRD) analysis showed that the desired intermetallic phase was obtained in single phase for each compound (Figure S1). The  $\text{H}_2$ -mediated isomerization of *cis*-ST into *trans*-ST was performed in the presence of these catalysts. When monometallic Rh/ $\text{SiO}_2$  was used, not only isomerization to *trans*-ST, but also overhydrogenation to diphenylethane (DPE) proceeded, lowering *trans* selectivity down to  $\approx 40\%$  (Figure 1).

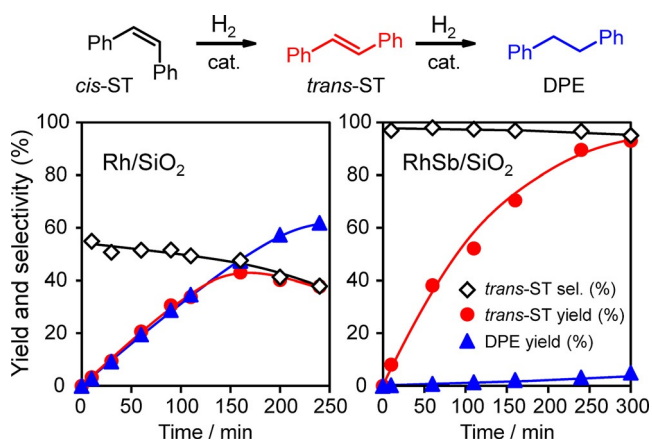


**Figure 1.** Time courses of *trans*-ST selectivity, *trans*-ST yield, and DPE yield in the liquid-phase hydrogen-mediated isomerization of *cis*-ST over Rh/ $\text{SiO}_2$  and RhSb/ $\text{SiO}_2$  catalysts.

In contrast, the RhSb/ $\text{SiO}_2$  catalyst effectively inhibited the overhydrogenation, affording 95% *trans* selectivity at full conversion. The *trans* selectivities of the prepared catalysts at 50% conversion were compared (Figure 2, red bars).

Intermetallic compounds RhIn, RhGa, and RhZn showed similar selectivities to monometallic Rh but lower selectivities than RhSb, RuSb, RhGe, and RhPb. Intermetallic RhSb exhibited the highest selectivity (97%). Interestingly, the selectivity order appeared to depend on the space group of the intermetallic phases:  $Pnma$  (orthorhombic, RhSb, RuSb, RhGe)  $>$   $P6/mmm$  (hexagonal, RhPb)  $>$   $Pm\bar{3}m$ ,  $Fm\bar{3}m$  (cubic, RhIn, RhGa, RhZn, Rh), suggesting that geometry affects selectivity. To further examine this geometric effect, *cis*- $\beta$ -methylstyrene (*cis*-MS), which bears a less sterically hindered alkenyl moiety than *cis*-ST, was isomerized. The resulting order of selectivity was similar to that of *cis*-ST (Figure 2, green bars). Furthermore, the obtained selectivities were lower than those of *cis*-ST for all catalysts, indicating that the steric hindrance around the alkenyl moiety contributed to the isomerization and/or hydrogenation. These results strongly suggest that geometric factors govern selectivity. The isomerization of *cis*-2-butene, which is the least sterically hindered inner alkene, was also assessed (Figure S2). Similarly

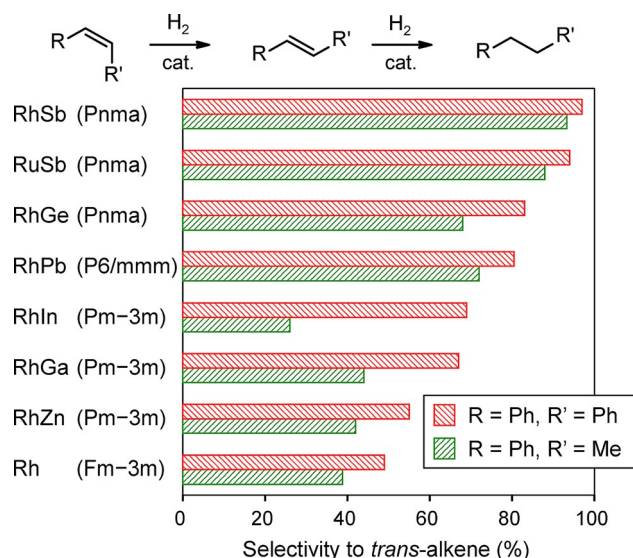


**Figure 2.** Selectivities to *trans*-alkenes during *cis*-ST and *cis*-MS isomerizations catalyzed by various  $\text{SiO}_2$ -supported Rh- and Ru-based intermetallic compounds and monometallic Rh under atmospheric pressure of  $\text{H}_2$ . Selectivities at 50% conversion are shown. The space group of the metallic phase appears in parentheses.

to ST and MS, RhSb exhibited the highest selectivity (83%), whereas the cubic compounds (RhZn, RhGa, and Rh) gave low selectivities (50, 49, and 43%, respectively).

Next, the effect of Rh electronic state on selectivity was investigated by evaluating a) the binding energy of the  $\text{Rh}3d_{5/2}$  emission, b) d band center, and c) vibrational frequency of linearly adsorbed CO (Figure S3a–c). No correlation was observed between the selectivities and these parameters (Figure S3d–f), indicating that the selectivity does not depend on the electronic state of Rh.

Intermetallic compound RhSb was characterized in detail to identify the geometric effect. Figure 3a shows a transmission electron microscopy (TEM) image of a  $\text{SiO}_2$ -supported intermetallic RhSb nanoparticle. The nanobeam diffraction (NBD) pattern of this nanoparticle showed a set of diffraction spots corresponding to an intermetallic RhSb single crystal oriented along the  $[1\bar{3}\bar{1}]$  direction (Figure 3b). The equilibrium crystal shape of RhSb (Figure 3c) was determined by Wulff construction<sup>[11]</sup> using surface energies (Table S1) of various RhSb low-index planes (Figure S4) estimated by DFT calculation. The RhSb crystal surface mainly comprised  $\{211\}$ ,  $\{020\}$ ,  $\{013\}$ , and  $\{102\}$  planes and the crystal shape agreed with the TEM image. Understanding of the geometric effect relies on an evaluation of exposed surface atomic arrangements. Figure 3d shows atomic arrangements at equilibrium crystal surfaces. Most planes displayed unique arrangements, in which Rh atoms were one-dimensionally aligned (1D-plane; e.g.,  $\{211\}$ ,  $\{020\}$ , and  $\{013\}$ ). The dominance of these 1D-planes may result from the wafer-like structure of  $Pnma$  crystals. Although bulk-terminated structures are shown here, note that almost no surface reconstruction occurred during geometry optimizations (Figure S5). Outermost Sb atoms (typically 0.2 Å) were only slightly lifted up. RhSb surfaces presented similar stability

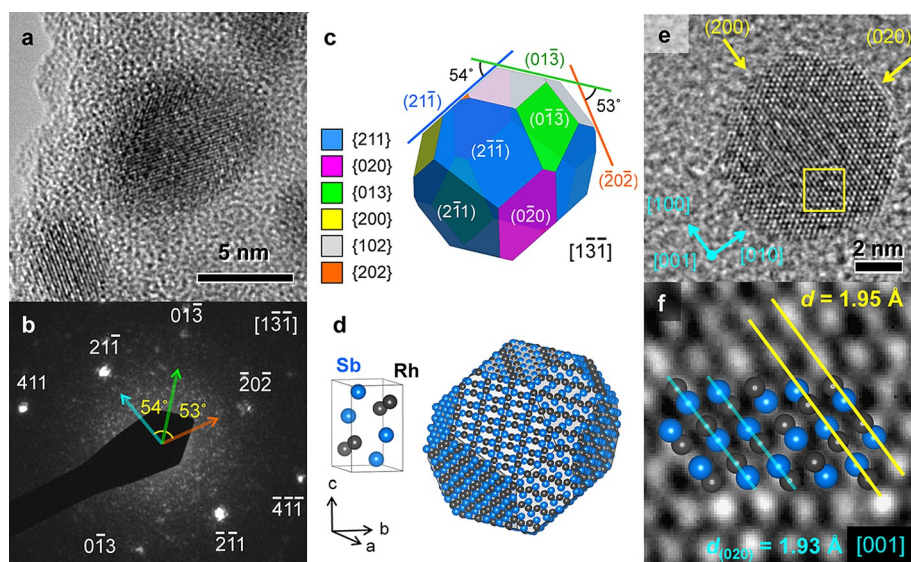


**Figure 3.** a) HR-TEM image of RhSb nanoparticles. b) NBD pattern focused on a single RhSb nanoparticle shown in the center of (a). c) Equilibrium crystal shape of RhSb determined by Wulff construction. The crystal orientation was equalized to that of the diffraction pattern (b). d) Crystal structure of RhSb showing the single unit cell (left) and surface atomic arrangements displayed in (c) (right). e) HR-TEM image of another RhSb nanoparticle. f) Close-up of the region delimited by the yellow square in (e). The crystal structure of RhSb viewed along the [001] direction is overlapped with the TEM image. Yellow and light blue lines represent experimental and reference d-spacings, respectively.

to PdGa-like intermetallic compounds, which may originate from covalent interactions between their metal components.<sup>[12]</sup>

Figure 3 e and f show a high-resolution TEM image of another RhSb nanoparticle and the magnification of the region designated by a yellow square, respectively. These images clearly displayed lattice fringes corresponding to (020) planes. Moreover, the observed atomic arrays closely matched the corresponding crystal structure viewed along the [001] direction. Figure 3 f shows that RhSb crystal structure continues to the outermost surface without any amorphous or deformed overlayers. This indicates that surface degradation of RhSb nanocrystals hardly occurs through TEM sample preparation using organic solvent in the air. Crystal terminations by (020) and (200) planes were also observed (3E), suggesting that these planes were exposed. These results were consistent with the exposure and dominance of 1D-planes in RhSb. In a wider-field TEM image, similar polyhedral nanocrystals with 5–10 nm sizes were mainly observed (Figure S6). However, a non-local characterization is necessary to obtain information about the entire RhSb catalyst. Therefore, a Fourier-transform infrared (FT-IR) analysis involving CO chemisorption was subsequently performed. Figure 4 shows FT-IR spectra of chemisorbed CO on RhSb/SiO<sub>2</sub> at various pressures. Some peaks assigned to linearly adsorbed CO<sup>[13]</sup> on Rh atoms appeared in the 2000–2030 cm<sup>-1</sup> region. No peak was observed below 1950 cm<sup>-1</sup>, indicating the absence of two-fold species and, thus, large Rh ensembles.<sup>[13]</sup> The peak positions remained almost unchanged when the intensity was lower than half of the saturation value ( $\leq 12$  Pa). Vibrational frequencies of CO chemisorbed on Rh atop sites of major 1D-planes observed in RhSb ((211), (020), and (013) planes) were estimated by DFT calculation. Models

presenting low CO coverage (1/8 full coverage for Rh) were adopted to exclude lateral interactions between CO molecules (Figure 4). Two geometrically different Rh sites (a and b, Figure 4) were investigated for the (211) plane.

Calculated frequencies for these surfaces (2009, 2010, 2023, and 2039 cm<sup>-1</sup> for (020), (013), (211)<sub>ar</sub> and (211)<sub>br</sub>, respectively) agreed with the observed peak (or shoulder) positions at low coverage ( $\leq 12$  Pa), strongly confirming the dominance of these surfaces. On the other hand, calculations involving CO chemisorption on bridge sites gave considerably lower values (1908–1922 cm<sup>-1</sup>, Table S2), which is consistent with the absence of bridged CO on RhSb. Similar analyses were performed for monometallic Rh/SiO<sub>2</sub> and RhGa/

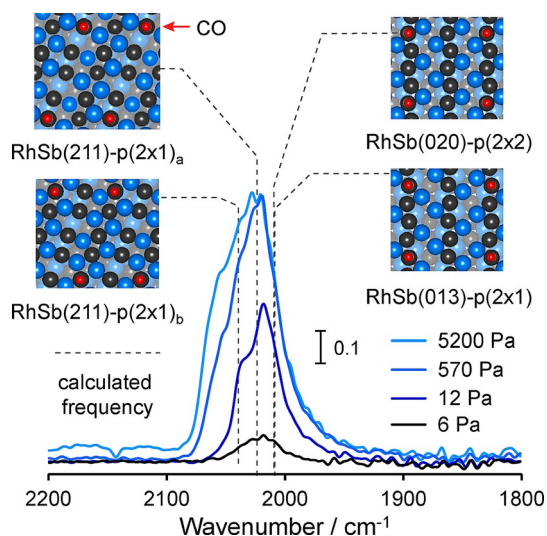


**Figure 4.** FT-IR spectra of CO chemisorbed on RhSb/SiO<sub>2</sub> at various CO pressures. Model structures of chemisorbed CO at low coverage (1/8 full coverage for Rh sites) and their calculated frequencies are also shown.

SiO<sub>2</sub>. For Rh/SiO<sub>2</sub>, calculated frequencies for CO chemisorbed on atop (2046 cm<sup>-1</sup>) and bridge sites (1930 cm<sup>-1</sup>) of Rh(111) surface correctly reproduced reported experimental values (2045 and 1925 cm<sup>-1</sup>, respectively,<sup>[14]</sup> Table S2). These calculations also agreed with experimental frequencies obtained in this study at low coverage (Figure S7 a), validating the computational approach. For RhGa/SiO<sub>2</sub>, the calculated frequencies of CO chemisorbed on (100), (110), and (111) planes were consistent with experimental results (Figure S7 b).

We now discuss the geometric role of 1D-plane on the selective isomerization. Hydrogen atom diffusion on the 1D-plane surface may be restricted to the direction of the Rh row. Indeed, on the RhSb(020) surface, DFT calculated activation barriers for hydrogen diffusion pathways amounted to 138–209 kJ mol<sup>-1</sup> across the Sb row, but 32–52 kJ mol<sup>-1</sup> along the Rh row (bridge-atop-bridge) (Figure 5).

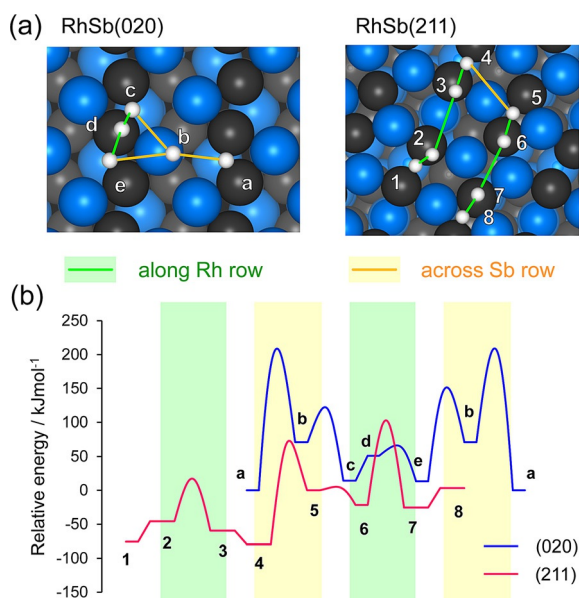


**Figure 5.** a) Hydrogen atom diffusion pathways over RhSb(020) and (211) surfaces and b) their corresponding energy diagrams. Geometry optimized stationary adsorption sites are designated as a–e and 1–8 (no stationary adsorption site was found between 2 and 3 or 6 and 7). Total energies of RhSb(020)-H(a) and RhSb(211)-H(5) slabs were set to zero. Energy barriers of representative steps (kJ mol<sup>-1</sup>): a → b (209), b → a (138), c → d (32), e → d (52), 2 → 3 (63), 3 → 2 (76), 4 → 5 (152), 6 → 7 (124), 7 → 6 (127).

The activation barriers for the Rh row exceeded the reported values for a monometallic Rh(111) surface ( $\approx 10$  kJ mol<sup>-1</sup>),<sup>[15]</sup> which is probably due to the absence of stable hollow sites and, consequently, the necessity to pass through relatively unstable atop sites.<sup>[15b]</sup> Similar calculations performed for the RhSb(211) surface provided significantly higher energy barriers, even for the pathway along Rh rows (63–127 kJ mol<sup>-1</sup>, Figure 5). This may be attributed to the longer Rh-Rh distances obtained on RhSb(211) than on (020) in addition to the presence of intercepting Sb atoms in the Rh rows. On the basis of these results, further analysis focused on RhSb(020) as an active surface.

Finally, the stereochemistry on 1D-planes was assessed by investigating the adsorption geometries of *cis* and *trans*-2-butenes as a model alkenes on the RhSb(020) surface and the energy profile of the isomerization. Generally, alkenes exhibit  $\pi$  and di- $\sigma$  adsorptions on metallic surfaces. The conventional Horiuti–Polanyi mechanism<sup>[16]</sup> suggests that the conversion of di- $\sigma$ -bonded alkenes into secondary alkyl intermediates is a key step in alkene isomerization and hydrogenation. However,  $\pi$ -bonded alkenes may also participate in the hydrogenation as has been proposed for Pt(111) surfaces.<sup>[17]</sup> Moreover,

because Rh and Sb rows were not straight but slightly zigzagged on the RhSb(020) surface, the adsorbate orientation was also geometrically distinguishable: methyl moieties faced left (*cis<sub>L</sub>*) or right (*cis<sub>R</sub>*) in *cis*-2-butene, whereas the *trans*-2-butene molecule lay parallel (*trans<sub>||</sub>*) or across the Rh row (*trans<sub>x</sub>*). In the present study, possible adsorption geometries of 2-butene (*cis/trans*,  $\pi$ /di- $\sigma$ , and orientations) and half-hydrogenated isobutyl intermediates were systematically considered (optimized structures are shown in Figure S8). The presence and absence of co-adsorbed hydrogen atoms was also taken into account. Figure 6 shows the adsorption energies of 2-butenes in various modes and representative optimized structures.

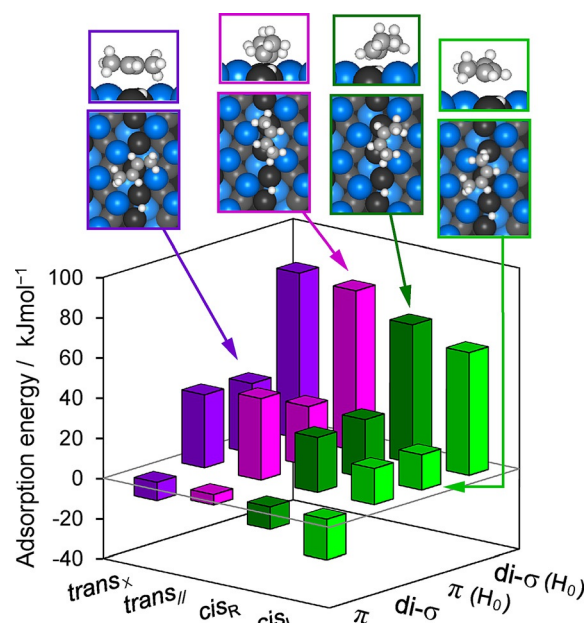


**Figure 6.** Adsorption energies of *cis* and *trans*-2-butenes on bare and hydrogen-adsorbed (designated by H<sub>0</sub>) RhSb(020) surfaces for various adsorption modes. Representative structures (side and top views), in which Rh, Sb, C, and H atoms appear in black, blue, gray, and white, respectively, are also shown.

Surprisingly, di- $\sigma$  adsorptions were energetically unfavorable compared to their  $\pi$  counterparts by  $\approx 40$  kJ mol<sup>-1</sup> regardless of the presence of hydrogen, in contrast with alkene adsorption on Pt(111) and Pd(111).<sup>[18]</sup> Because the Rh–C bond length should be shorter for the di- $\sigma$  adsorption than for the  $\pi$  adsorption, repulsion between methyl moieties and the slightly uplifted Sb atoms may have caused molecular deformation and/or destabilization. *cis* Conformations were more favorable than *trans* isomers regardless of orientation and bonding style. This may stem from the ability of *cis* isomers to tilt their molecular plane toward the surface to reduce steric repulsion, which is unavoidable in *trans* conformations.<sup>[19]</sup> The presence of adsorbed hydrogen gave more positive adsorption energies, as reported for the Pt(111) surface,<sup>[19b]</sup> without changing their order for various modes. This increase in adsorption energy may result from the hydrogen coverage-induced decrease in

surface energy. We calculated adsorption energies of 2-butenes also for a bare (211) surface. Much more positive adsorption energies than those for (020) surface were obtained (14–20 and 37–58 kJ mol<sup>-1</sup> for  $\pi$  and di- $\sigma$  modes, respectively, Figure S9). This unfavored adsorption is probably due to its small surface energy (Table S1), i.e., being stable surface. Our attempt for temperature-programmed desorption of 2-butenes on RhSb/SiO<sub>2</sub> resulted in rapid desorption upon evacuation even at room temperature (data not shown) and failed to estimate an experimental adsorption energy. However, this rapid desorption is consistent with the positive or slightly negative adsorption energies in Figure 6 and S9. Figure 7 shows the energy diagram for 2-butene isomerization over RhSb(020) with several adsorbate structures. This diagram addresses  $cis_L$ – $trans_{//}$  (solid lines) and  $cis_R$ – $trans_X$  isomerizations (dotted lines) involving  $\pi$  adsorption via isobutyl intermediates and C–C rotation. Typically, hydrogen atoms are assumed to access the alkenyl carbons from the bottom ( $H_0$ -TS<sub>1</sub>-H, see yellow arrow in 2). In  $cis$  conformations, one of the two alkenyl carbon atoms and the neighboring Rh–Rh bridge site are sterically blocked by one methyl group. Therefore, the hydrogen atom preferentially accesses the “open” side of the neighboring bridge site and/or the alkenyl carbon atoms rather than their blocked side. In the  $cis_L$  conformer, hydrogen access to the blocked side of the neighboring Rh–Rh bridge site (yellow arrow in 2') requires skeletal deformation (methyl rotation) and tilting of 2-butene at transition state TS<sub>1</sub>, resulting in a higher energy barrier (66 kJ mol<sup>-1</sup>, green solid line through 2') than for the open side (49 kJ mol<sup>-1</sup>, blue solid line through 2). A similar situation is also observed for the  $cis_R$  conformation (61 kJ mol<sup>-1</sup>, blue dotted line through 7). Hydrogen attack to  $cis_L$ -2-butene generates an isobutyl intermediate (4) via transition state TS<sub>2</sub> with an activation energy of 44 kJ mol<sup>-1</sup>. Isomerization to  $trans_{//}$ -2-butene proceeds via C–C rotation (TS<sub>3</sub>,  $E_a$  = 10 kJ mol<sup>-1</sup>) and subsequent  $\beta$ -H (orange) elimination (TS<sub>2</sub>',  $E_a$  = 18 kJ mol<sup>-1</sup>). The blocking methyl group may also hinder additional hydro-

gen attack to the isobutyl intermediate from the opposite side, minimizing overhydrogenation to alkane. The formed  $trans_{//}$ -2-butene can desorb directly into the gas phase because of the absence of activation barrier. Hydrogen atoms do not access  $trans_{//}$ -2-butene (6) because both alkenyl carbon atoms are blocked by the methyl groups. Both alkenyl carbon atoms are open in  $trans_X$ -2-butene, making the two-atom hydrogenation possible. However, this process is limited because  $trans_X$ -2-butene adsorption is less energetically favorable than other conformations (Figure 6 and 7). Applying Boltzmann distribution to adsorption energy difference between  $cis_L$  and  $trans_X$  (described below;  $E_{cis_L} - E_{trans_X} = \Delta E = 12$  kJ mol<sup>-1</sup>) yields 45-fold difference in adsorbate ratio even at 373 K, which is sufficient to ignore the reverse reaction [Eq. (1)]:

$$\frac{[cis_L - \pi]/[cis_L(g)]}{[trans_X - \pi]/[trans_X(g)]} = \frac{\exp(E_{cis_L}/RT)}{\exp(E_{trans_X}/RT)} = \exp(\Delta E/RT) \quad (1)$$

The isomerization process via di- $\sigma$  bonded 2-butenes was also considered but their hydrogenations exhibited dramatically higher activation energies (75–132 kJ mol<sup>-1</sup>, Figure S10) than those of  $\pi$ -bonded alkenes. Di- $\sigma$  bonded species thus displayed significantly higher energy barriers for adsorption and hydrogenation, ruling out their contribution to this catalysis.

Thus, several combined effects play a critical role on the selective  $cis$ – $trans$  isomerization of 2-butene on the RhSb(020) surface. a) Hydrogen atom diffusion on the surface is restricted to the direction of the one-dimensionally aligned Rh row. b)  $cis$ -2-Butene adsorption is considerably more favorable than that of  $trans$ -2-butene. c) In  $cis$  conformations, steric hindrance from the methyl group limits hydrogen atom access to one side of the alkene (Scheme 1a).

The second effect promotes the desorption of the resulting  $trans$  isomer in addition to enhancing the third effect, which enables the one-atom hydrogenation and isomerization, while inhibiting the two-atom hydrogenation (Scheme 1c). This

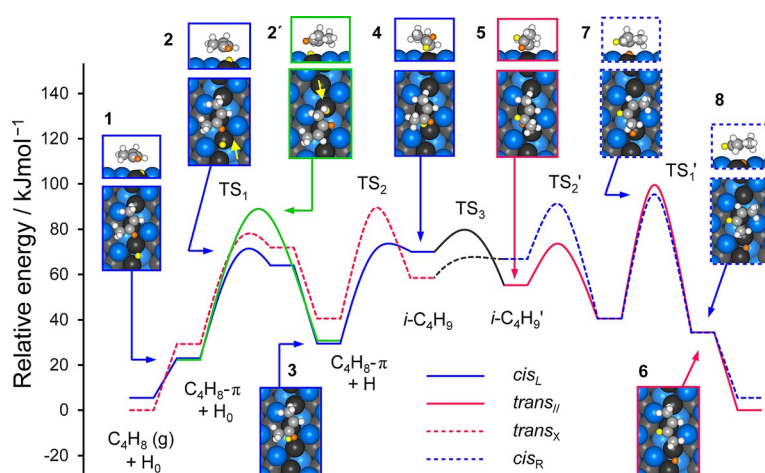
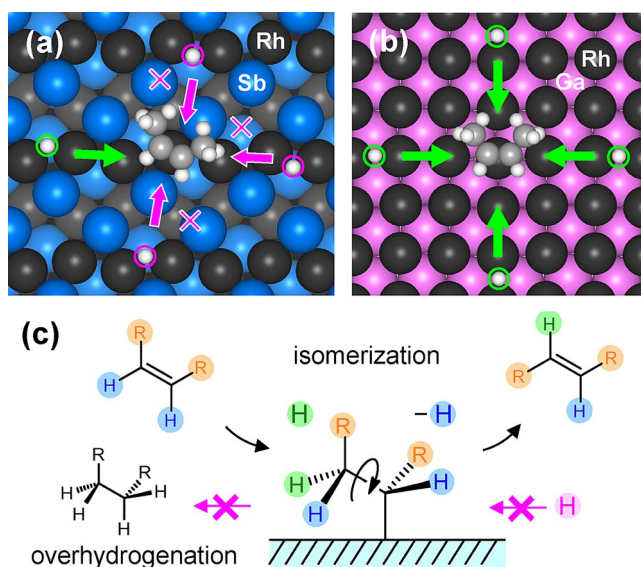


**Figure 7.** Energy diagram for the  $cis$ – $trans$  isomerization of 2-butene on the RhSb(020) plane and adsorbate structures (side and top views, 1–8). Total energy of gas-phase  $trans$ -2-butene and hydrogen-adsorbed RhSb(020) slab was set to zero. Hydrogen atoms involved in the isomerization appear in yellow and orange. The green line corresponds to hydrogen access to the alkenyl carbon of  $cis_L$ -2-butene from the top, which is sterically hindered by the methyl group.

highly selective isomerization catalysis relies on the specific and regular surface atomic arrangement of the orthorhombic  $Pnma$  intermetallic compound. The characteristic zigzag alignment of the Rh atoms also contributes to the surface stereochemistry. A straight alignment may result in equal steric hindrance of the alkenyl carbon atoms from two alkyl groups, preventing geometric differentiation between open or blocked. Note that the overall selectivity should be a weighted superposition of the different contribution of each plane; for RhSb, (211), (020), and (013) planes. As discussed above, since (211) plane can be regard-



**Scheme 1.** Geometric restriction of hydrogen access to *cis*-2-butene on a) 1D and b) Rh-terminated planes such as RhSb (020) and RhGa(100), respectively. c) Selective *cis*–*trans* alkene isomerization without overhydrogenation to alkane.

ed as almost inactive due to the significantly high hydrogen diffusion barriers and positive 2-butene adsorption energies, its contribution to the catalysis may be negligible. Therefore, overall selectivity depends strongly on the nature of (020) and (013) planes. For (013) surface, the nature and surface stereochemistry are likely to be similar to those for (020) surface because its surface energy (Table S1) and atomic arrangement (Figure 3 and S4) are almost identical to those of (020) surface. This means that the overall selectivity is governed by a portion of *Pnma* crystal facets.

For monometallic Rh, because hydrogen atoms can access the alkenyl moiety from several orientations, the two-atom hydrogenation easily occurs, explaining the low selectivity. Similarly for other cubic *Pm* $\bar{3}$ *m* intermetallic compounds such as RhGa, RhIn, and RhZn, the two-atom hydrogenation may proceed on Rh-terminated (100) surfaces (Scheme 1b and Figure S7b). In this catalytic system, selectivity also depends on the degree of steric hindrance from the alkyl moiety of adsorbed alkene, which is consistent with the deviations in selectivity between *cis*-ST and *cis*-MS isomerizations (Figure 2). The phenyl group of ST displays a significantly higher steric effect than the methyl group of MS, giving rise to higher selectivity. We reported in the previous work that RhSb was almost inactive for semihydrogenation of alkyne to alkene. This supports that RhSb surface catalyzes one-atom hydrogenation but not two-atom hydrogenation. More likely, for alkynes on 1D-plane, hydrogen access to the alkenyl carbons may be blocked completely by two alkyl moieties on an extension of the C–C triple bond.

Although we here demonstrated the case of an ideal surface, slight surface modification might be caused in the actual reaction condition by other factors such as solvent. Moreover, some nanoparticles may not show an ideal Wulff polyhedron

because contribution of corners and edges cannot be ignored for nanoparticles smaller than 10 nm.<sup>[20]</sup> However, the wafer like crystal structure of *Pnma* RhSb should expose 1D-like surface for most Miller indices excepting {200} planes. The concept of selective isomerization on 1D-plane is simple and would essentially be applicable to the actual surface.

## Conclusions

The origin of the stereochemical *cis*–*trans* alkene conversion on Rh-based intermetallic compounds was investigated using multiple techniques combined with DFT calculations. The *trans*-alkene selectivity strongly depends on geometric factors, such as space group of the intermetallic phases and alkene size, instead of their electronic states. Highly selective intermetallic compounds, such as RhSb, exhibit an orthorhombic *Pnma* structure, of which surfaces are dominated by planes consisting of one-dimensionally aligned Rh rows separated by Sb (1D-planes) with minimum surface relaxation. Geometric constraints on 1D-planes and steric hindrance from one alkyl group of *cis*-alkene effectively limit hydrogen access to the alkenyl carbon to one direction, which enables the one-atom hydrogenation hence isomerization, while inhibiting the two-atom hydrogenation to alkane. This unprecedented surface stereochemistry largely relies on the unique and highly ordered surface atomic arrangement of the intermetallic compounds, which is rare in other inorganic materials. This study provides the first example of selective stereochemical conversion controlled by surface order. The gained insight is expected to open new horizons for several fields, such as catalytic chemistry, surface science, stereochemistry, and materials science.

## Experimental Section

### Catalyst preparation

Silica-supported Rh or Ru catalysts (Rh/SiO<sub>2</sub>, Ru/SiO<sub>2</sub>) were prepared by a pore-filling impregnation. An aqueous Rh(NO<sub>3</sub>)<sub>3</sub> (N.E. ChemCat Corp., 99%) or RuCl<sub>3</sub> solution (Furuya Metal Co., Ltd., 99%) was added to dried silica gel (Cariact G-6, Fuji Silysia Ltd.) The metal solution volume was calculated to fill silica gel pores and achieve 3 wt% metal loading. The mixture was sealed overnight at room temperature using a piece of plastic film, dried over a hot plate at 373 K, and calcined under dry air at 723 K for 4 h. The catalyst was subsequently reduced under H<sub>2</sub> flow (60 mL min<sup>-1</sup>, 99.9995%, Taiyo Nippon Sanso Corp.) for 2 h at 823 (Rh) or 723 K (Ru).

Silica-supported intermetallic catalysts (RhM/SiO<sub>2</sub> with M = Ga, Ge, In, Pb, Sb, Zn; RuSb/SiO<sub>2</sub>) were prepared by successive impregnations of Rh/SiO<sub>2</sub> or Ru/SiO<sub>2</sub>. The RhSb catalyst was obtained by adding an aqueous SbCl<sub>3</sub> solution (99%, Kanto) to Rh/SiO<sub>2</sub> to adjust the Rh/Sb atomic ratio to 1. The mixture was sealed by a piece of plastic film overnight at room temperature, dried over a hot plate, and reduced under H<sub>2</sub> flow at 1073 K for 1 h. Other intermetallic catalysts (RhGa, RhGe, RhIn, RhPb, and RhZn) were prepared by a similar procedure at various reduction temperatures using Ga(NO<sub>3</sub>)<sub>3</sub>·8H<sub>2</sub>O (Wako, 99%, 1073 K), (NH<sub>4</sub>)<sub>2</sub>GeF<sub>6</sub> (Aldrich, 99%, 1073 K), InCl<sub>3</sub>·4H<sub>2</sub>O (Wako, 723 K), Pb(NO<sub>3</sub>)<sub>2</sub> (Kanto, 99%,

1023 K), and  $\text{Zn}(\text{NO}_3)_2 \cdot 2\text{H}_2\text{O}$  (Wako, 99%, 1073 K), respectively. Bulk intermetallic catalysts ( $\text{RhM}$ ;  $\text{M} = \text{Ga}, \text{Ge}, \text{In}, \text{Sb}$ ) were prepared by arc melting of pure metal beads at a 1:1 atomic ratio under Ar atmosphere. The resulting ingots were crushed into fine powder in the air.

### Reaction conditions

Isomerizations of *cis*-stilbene (*cis*-ST) and *cis*- $\beta$ -methylstyrene (*cis*-MS) were carried out in a 100 mL three-neck round bottom flask equipped with a reflux condenser and a gas balloon. Prior to the reaction, the catalyst (100 mg) was reduced under flowing  $\text{H}_2$  (60 mL  $\text{min}^{-1}$ ) for 1 h in the reactor heated to 673 K using a mantle heater. The reactor was subsequently cooled to room temperature and the atmosphere was completely replaced by dry Ar. A THF solution (5.0 mL) of *cis*-ST or *cis*-MS (5 mmol, TCI, 99%) was added to the reactor through a silicone septum. The reaction was initiated at 298 K by flowing  $\text{H}_2$  at 100 mL  $\text{min}^{-1}$  for 1 min and 5 mL  $\text{min}^{-1}$  afterward. Products present in the liquid phase were quantified using a flame ionization detection gas chromatograph (Shimadzu, GC-14B) equipped with a capillary column (GL Sciences, TC-70, 0.25 mm  $\times$  60 m). The *trans*-alkene selectivity at 50% conversion was determined using 50 mg of catalyst and 1 mmol of *cis*-alkenes.

*cis*-2-Butene was isomerized in a continuous fixed-bed flow reactor (quartz, I.D. = 6 mm). Prior to the reaction, the catalyst (10 mg) was reduced under  $\text{H}_2$  flow (60 mL  $\text{min}^{-1}$ ) in the reactor at 623 K for 1 h and allowed to cool to 373 K under He flow (60 mL  $\text{min}^{-1}$ ). The reaction was initiated by flowing the 2:1:15 *cis*-2-butene/ $\text{H}_2$ /He reaction mixture (total flow rate: 90 mL  $\text{min}^{-1}$ ) at 373 K. Products present in the gas phase were analyzed using a thermal conductivity detection gas chromatograph (Shimadzu, GC-8A) equipped with a packed column (VZ-10, 3 mm  $\times$  6 m).

### Characterization

Crystal structures were examined by powder X-ray diffraction (XRD) under  $\text{Cu}_{\text{K}\alpha}$  radiation using a Rigaku RINT2400 apparatus. Difference XRD patterns were obtained by subtracting the silica support pattern from those of the supported catalysts to give a flat baseline. Transmission electron microscopy (TEM) measurements were conducted using a JEOL JEM-2010F instrument at an accelerating voltage of 200 kV. All TEM specimens were prepared by sonicating the samples in tetrachloromethane and dispersing them on a copper grid by an ultrathin carbon film supported. Nanobeam diffraction patterns were acquired at a camera distance of 30 cm. The camera constant was calibrated using a gold standard for reflection index determination. X-ray photoelectron spectra (XPS) were recorded using an ULVAC PHI 5000 VersaProbe spectrometer. Catalysts were pressed into a pellet and reduced under  $\text{H}_2$  flow (60 mL  $\text{min}^{-1}$ ) at 873 K in a quartz reactor for 1 h. Spectra were obtained under  $\text{Al}_{\text{K}\alpha}$  X-ray radiation using the C 1s peak (248.8 eV) to calibrate the binding energy. Valence band XPS measurements were performed using unsupported bulk catalysts because their supported counterparts produced extremely low valence band intensities. Bulk catalysts exhibited similar selectivities to their corresponding supported catalysts. For example, bulk RhSb showed 96% *trans* selectivity at 50% conversion of *cis*-ST. The d band center ( $C_d$ ) was defined as the position of the vertical line bisecting the d band area. Fourier-transform infrared (FT-IR) spectra of adsorbed CO were obtained using a JASCO FT/IR-430 spectrometer in transmission mode. A self-supporting catalyst wafer (50 mg  $\text{cm}^{-2}$ ) was placed in a quartz cell equipped with  $\text{CaF}_2$  windows and con-

nected to a glass circulation system. The catalyst was reduced under  $\text{H}_2$  flow at 673 K for 0.5 h, evacuated at the same temperature for 0.5 h, and cooled to room temperature. Next, a spectrum was recorded as a baseline for subsequent measurements. A  $10^1$ – $10^3$  Pa CO was introduced stepwise at room temperature. All spectra were acquired at a 4  $\text{cm}^{-1}$  resolution.

### Computational Details

Periodic density functional theory (DFT) calculations, except frequency calculations, were performed using the CASTEP code<sup>[21]</sup> with Vanderbilt-type ultrasoft pseudopotentials<sup>[22]</sup> and a revised Perdew–Burke–Ernzerhof exchange–correlation functional (RPBE)<sup>[23]</sup> based on the generalized gradient approximation (GGA). The plane-wave basis set was truncated at a kinetic energy of 370 eV. A Fermi smearing of 0.1 eV was utilized. The reciprocal space was sampled using a *k*-point mesh with a typical spacing of 0.04  $\text{\AA}^{-1}$  generated by the Monkhorst–Pack scheme.<sup>[24]</sup>

Geometry optimizations were performed in supercell structures using periodic boundary conditions. Surfaces were modeled using 6 atomic layer-thick metallic slabs. Surface energies were calculated using (1  $\times$  1) unit cells with a 10  $\text{\AA}$  vacuum region separating the two surfaces under symmetry restrictions. When any adsorbate (CO, H, and/or *cis*- or *trans*-2-butenes) was included, (2  $\times$  1) (RhSb(211) and RhSb(013)), (2  $\times$  2) (RhSb(020)), or (3  $\times$  3) (Rh(111), RhGa(100), RhGa(110), and RhGa(111)) unit cells with a 13  $\text{\AA}$  vacuum region were used without symmetry restrictions. Atomic coordinates were fully relaxed, while the lattice constants were fixed. Convergence criteria comprised a) a self-consistent field (SCF) tolerance of  $2.0 \times 10^{-6}$  eV/atom, b) an energy tolerance of  $1.0 \times 10^{-5}$  eV/atom, c) a maximum force tolerance of 0.05 eV  $\text{\AA}^{-1}$ , and d) a maximum displacement tolerance of  $1.0 \times 10^{-3}$   $\text{\AA}$  for structure optimization and energy calculation.

The adsorption energy was defined as Equation (2):

$$E_{\text{ad}} = E_{\text{A-s}} - (E_{\text{s}} + E_{\text{A}}) \quad (2)$$

For which  $E_{\text{A-s}}$  is the energy of the slab with the adsorbate,  $E_{\text{A}}$  is the total energy of the free adsorbate, and  $E_{\text{s}}$  is the total energy of the bare slab. The adsorption energy with a hydrogen-adsorbed slab was calculated using the total energy of hydrogen-adsorbed slab ( $E_{\text{SH}}$ ) instead of  $E_{\text{s}}$ .

Surface energies of various planes, except RhSb(200), were estimated using Equation (3):

$$\gamma = \lim_{n \rightarrow \infty} \frac{1}{2A} [E_{\text{s}} - nE_{\text{B}}] \quad (3)$$

For which  $E_{\text{B}}$  is the energy of bulk unit cell,  $A$  is the surface area,  $n$  is the number of layers, and  $N$  is the number of unit cells in the slab. Surface energy calculations were conducted for densely packed low-index RhSb(111), (102), (112), (211), (200), (020), (020), and (013) planes. These surface energies converged within 6 or 7 atomic layers for several surfaces (Table S1). Unlike other planes, RhSb(200) displays one surface consisting of Rh atoms only (RhSb(200)<sub>Rh</sub>) and another one composed of Sb atoms only (RhSb(200)<sub>Sb</sub>). This procedure gave averaged surface energies for RhSb(200)<sub>Rh</sub> ( $\gamma_{\text{Rh}}$ ) and RhSb(200)<sub>Sb</sub> ( $\gamma_{\text{Sb}}$ ) instead of individual contributions. Individual surface energies can be estimated using a non-stoichiometric slab model in which both surfaces are terminated by an identical plane (6). According to literature<sup>[11b,c]</sup> for example,

$\gamma_{\text{Rh}}$  for the Rh-terminated slab is described as Equation (4):

$$\gamma_{\text{Rh}} = \frac{1}{2A} [E_s - N_{\text{Sb}} \mu_{\text{RhSb}} - \Delta N \mu_{\text{Rh}}] \quad (4)$$

For which  $N_{\text{Sb}}$  is the number of Sb atoms in the slab,  $\Delta N$  is the excess of Rh atoms relative to Sb atoms,  $\mu_{\text{RhSb}}$  is the chemical potential of bulk RhSb, and  $\mu_{\text{Rh}}$  is the chemical potential of Rh, respectively.

Because of the bulk intermetallic compound stability against decomposition, the chemical potential  $\mu_{\text{Rh}}$  should lie within this range:

$$\mu_{\text{Rh(bulk)}} - |\Delta H_{\text{RhSb}}| \leq \mu_{\text{Rh}} \leq \mu_{\text{Rh(bulk)}} \quad (5)$$

Therefore,  $\gamma_{\text{Rh}}$  is expected to range within:

$$\begin{aligned} \frac{1}{2A} [E_s - N_{\text{Sb}} \mu_{\text{RhSb}} - \Delta N (\mu_{\text{Rh(bulk)}} - |\Delta H_{\text{RhSb}}|)] &\leq \gamma_{\text{Rh}} \\ &\leq \frac{1}{2A} [E_s - N_{\text{Sb}} \mu_{\text{RhSb}} - \Delta N \mu_{\text{Rh(bulk)}}] \end{aligned} \quad (6)$$

For which  $\Delta H_{\text{RhSb}}$  is the formation enthalpy of RhSb.

The transition state (TS) search was performed using the complete LST/QST method.<sup>[25]</sup> A linear synchronous transit (LST) maximization was performed, followed by an energy minimization in the directions conjugating to the reaction pathway. The approximated TS structure was subjected to a quadratic synchronous transit (QST) maximization with conjugate gradient minimization refinements. This cycle was repeated until a stationary point was found. The convergence criterion for TS calculations was set to a root-mean-square force tolerance of 0.10 eV Å<sup>-1</sup>.

Frequency calculations of adsorbed CO molecules were conducted from geometry optimized structures using the DMol<sup>3</sup> code.<sup>[26]</sup> These calculations involved the RPBE functional, a double-numeric quality basis set with polarization functions (DNP, comparable to Gaussian 6-311G\*\*)<sup>[27]</sup> with a real-space cutoff of 4.2 Å, DFT semi-core pseudopotential core treatment,<sup>[28]</sup> and a Fermi smearing of 0.1 eV. The SCF convergence was accelerated using the iterative scheme proposed by Kresse and Furthmüller.<sup>[29]</sup> The partial Hessian matrix including C and O atoms was computed to evaluate the harmonic frequencies for adsorbed CO. All computed harmonic frequencies were scaled by an empirical factor of 1.0624, which corresponds to the ratio of experimental<sup>[30]</sup> and computed values for gas-phase CO (2143 cm<sup>-1</sup>/2017 cm<sup>-1</sup>).

## Acknowledgements

This work was supported by a Japan Society for the Promotion of Science KAKENHI (Grant Number 23360353). We are grateful to the Center for Advanced Materials Analysis of Tokyo Institute of Technology for the aid of TEM observations.

**Keywords:** atomic arrangement · intermetallic compound · isomerization · stereochemistry · surface chemistry

- [1] a) S. Oudeyer, J. F. Briere, V. Levacher, *Eur. J. Org. Chem.* **2014**, 6103–6119; b) Y. L. Liu, J. S. Yu, J. Zhou, *Asian J. Org. Chem.* **2013**, 2, 194–206; c) X. Wang, K. Sun, Y. H. Lv, F. J. Ma, G. Li, D. H. Li, Z. H. Zhu, Y. Q. Jiang, F. Zhao, *Chem. Asian J.* **2014**, 9, 3413–3416.

- [2] a) J. Mlynarski, S. Bas, *Chem. Soc. Rev.* **2014**, 43, 577–587; b) T. Ohkuma, *J. Synth. Org. Chem. Jpn.* **2007**, 65, 1070–1080.  
 [3] a) Z. An, J. He, Y. Dai, C. G. Yu, B. Li, J. He, *J. Catal.* **2014**, 317, 105–113; b) J. M. Thomas, R. Raja, *Acc. Chem. Res.* **2008**, 41, 708–720; c) M. Nasr-Esfahani, I. Mohammadpoor-Baltork, A. R. Khosropour, M. Moghadam, V. Mirkhani, S. Tangestaninejad, H. A. Rudbari, *J. Org. Chem.* **2014**, 79, 1437–1443.  
 [4] a) M. Studer, H. U. Blaser, C. Exner, *Adv. Synth. Catal.* **2003**, 345, 45–65; b) C. J. Baddeley, *Top. Catal.* **2003**, 25, 17–28.  
 [5] a) E. J. Creighton, S. D. Ganeshie, R. S. Downing, H. Vanbekkum, *J. Chem. Soc. Chem. Commun.* **1995**, 1859–1860; b) E. J. Creighton, S. D. Ganeshie, R. S. Downing, H. vanBekkum, *J. Mol. Catal. A* **1997**, 115, 457–472.  
 [6] a) S. S. Kim, T. J. Pinnavaia, R. Damavarapu, *J. Catal.* **2008**, 253, 289–294; b) K. Smith, S. D. Roberts, G. A. Ei-Hiti, *Org. Biomol. Chem.* **2003**, 1, 1552–1559.  
 [7] J. H. Westbrook, R. L. Fleischer, *Magnetic, Electrical and Optical Properties and Applications of Intermetallic Compounds*, Wiley, **2000**.  
 [8] a) Z. Nawaz, F. Baksh, J. Zhu, F. Wei, *J. Ind. Eng. Chem.* **2013**, 19, 540–546; b) S. Scirè, G. Burgio, C. Crisafulli, S. Minico, *Appl. Catal. A* **2004**, 274, 151–157.  
 [9] a) M. Armbrüster, M. Behrens, F. Cinquini, K. Föttinger, Y. Grin, A. Haghofer, B. Klötzer, A. Knop-Gericke, H. Lorenz, A. Ota, S. Penner, J. Prinz, C. Rameshan, Z. Revay, D. Rosenthal, N. Rupprechter, P. Sautet, R. Schlögl, L. D. Shao, L. Szentmiklosi, D. Teschner, D. Torres, R. Wagner, R. Widmer, G. Wowsnick, *ChemCatChem* **2012**, 4, 1048–1063; b) M. Armbrüster, K. Kovnir, M. Behrens, D. Teschner, Y. Grin, R. Schlögl, *J. Am. Chem. Soc.* **2010**, 132, 14745–14747; c) K. Kovnir, M. Armbrüster, D. Teschner, T. V. Venkov, L. Szentmiklosi, F. C. Jentoft, A. Knop-Gericke, Y. Grin, R. Schlögl, *Surf. Sci.* **2009**, 603, 1784–1792.  
 [10] S. Furukawa, A. Yokoyama, T. Komatsu, *ACS Catal.* **2014**, 4, 3581–3585.  
 [11] a) G. Wulff, *Z. Kristallogr. Mineral.* **1901**, 34, 449–530; b) N. Moll, A. Kley, E. Pehlke, M. Scheffler, *Phys. Rev. B* **1996**, 54, 8844–8855; c) A. Dannenberg, M. E. Gruner, A. Hucht, P. Entel, *Phys. Rev. B* **2009**, 80, 245438.  
 [12] D. Rosenthal, R. Widmer, R. Wagner, P. Gille, M. Armbrüster, Y. Grin, R. Schlögl, O. Groning, *Langmuir* **2012**, 28, 6848–6856.  
 [13] K. Tomishige, K. Asakura, Y. Iwasawa, *J. Catal.* **1994**, 149, 70–80.  
 [14] A. C. Yang, C. W. Garland, *J. Phys. Chem.* **1957**, 61, 1504–1512.  
 [15] a) M. Mavrikakis, J. Rempel, J. Greeley, L. B. Hansen, J. K. Nørskov, *J. Chem. Phys.* **2002**, 117, 6737–6744; b) B. S. Bunick, G. J. Kramer, *J. Catal.* **2006**, 242, 309–318.  
 [16] J. Horiti, M. Polanyi, *Trans. Faraday Soc.* **1934**, 30, 1164–1172.  
 [17] P. S. Cremer, X. C. Su, Y. R. Shen, G. A. Somorjai, *J. Am. Chem. Soc.* **1996**, 118, 2942–2949.  
 [18] A. Valcárcel, A. Clotet, J. M. Ricart, F. Delbecq, P. Sautet, *Surf. Sci.* **2004**, 549, 121–133.  
 [19] a) I. Lee, F. Delbecq, R. Morales, M. A. Albitet, F. Zaera, *Nat. Mater.* **2009**, 8, 132–138; b) F. Delbecq, F. Zaera, *J. Am. Chem. Soc.* **2008**, 130, 14924–14925.  
 [20] a) H. Graoui, S. Giorgio, C. R. Henry, *Philos. Mag. B* **2001**, 81, 1649; b) S. W. Wang, L. M. Falicov, A. W. Searcy, *Surf. Sci.* **1984**, 143, 609.  
 [21] M. D. Segall, P. J. D. Lindan, M. J. Probert, C. J. Pickard, P. J. Hasnip, S. J. Clark, M. C. Payne, *J. Phys. Condens. Matter* **2002**, 14, 2717–2744.  
 [22] D. Vanderbilt, *Phys. Rev. B* **1990**, 41, 7892–7895.  
 [23] a) B. Hammer, L. B. Hansen, J. K. Nørskov, *Phys. Rev. B* **1999**, 59, 7413–7421; b) Y. K. Zhang, W. T. Yang, *Phys. Rev. Lett.* **1998**, 80, 890–890.  
 [24] H. J. Monkhorst, J. D. Pack, *Phys. Rev. B* **1976**, 13, 5188–5192.  
 [25] a) N. Govind, M. Petersen, G. Fitzgerald, D. King-Smith, J. Andzelm, *Comput. Mater. Sci.* **2003**, 28, 250–258; b) T. A. Halgren, W. N. Lipscomb, *Chem. Phys. Lett.* **1977**, 49, 225–232.  
 [26] B. Delley, *J. Chem. Phys.* **1990**, 92, 508–517.  
 [27] Y. Inada, H. Orita, *J. Comput. Chem.* **2008**, 29, 225–232.  
 [28] B. Delley, *Phys. Rev. B* **2002**, 66, 155125.  
 [29] G. Kresse, J. Furthmüller, *Phys. Rev. B* **1996**, 54, 11169–11186.  
 [30] D. Scarano, S. Bordiga, C. Lamberti, G. Spoto, G. Ricchiardi, A. Zecchina, C. O. Areal, *Surf. Sci.* **1998**, 411, 272–285.

Received: July 22, 2015

Published online on October 26, 2015